Ks-BAND DETECTION OF THERMAL EMISSION AND COLOR CONSTRAINTS TO CoRoT-1b: A LOW-ALBEDO PLANET WITH INEFFICIENT ATMOSPHERIC ENERGY REDISTRIBUTION AND A TEMPERATURE INVERSION*

JUSTIN C. ROGERS[1,2], DÁNIEL APAI[2], MERCEDES LÓPEZ-MORALES[3,6], DAVID K. SING[4], AND ADAM BURROWS[5]
[1] Department of Physics and Astronomy, Johns Hopkins University, 366 Bloomberg Center, 3400 N. Charles Street, Baltimore, MD 21218, USA; rogers@pha.jhu.edu
[2] Space Telescope Science Institute, 3700 San Martin Drive, Baltimore, MD 21218, USA
[3] Department of Terrestrial Magnetism, Carnegie Institution of Washngton, 5241 Broad Branch Rd. NW, Washington, DC 20015, USA
[4] UPMC Univ Paris 06, CNRS, Institut d'Astrophysique de Paris, 98bis boulevard Arago, F-75014 Paris, France
[5] Department of Astrophysical Sciences, Princeton University, Peyton Hall, Princeton, NJ 08544, USA

ABSTRACT

We report the detection in Ks-band of the secondary eclipse of the hot Jupiter CoRoT-1b from time series photometry with the ARC 3.5 m telescope at Apache Point Observatory. The eclipse shows a depth of $0.336 \pm 0.042\%$ and is centered at phase $0.5022^{+0.0023}_{-0.0027}$, consistent with a zero eccentricity orbit ($e \cos \omega = 0.0035^{+0.0036}_{-0.0042}$). We perform the first optical to near-infrared multi-band photometric analysis of an exoplanet's atmosphere and constrain the reflected and thermal emissions by combining our result with the recent 0.6, 0.71, and 2.09 μm secondary eclipse detections by Snellen et al., Gillon et al., and Alonso et al. Comparing the multi-wavelength detections to state-of-the-art radiative-convective chemical-equilibrium atmosphere models, we find the near-infrared fluxes difficult to reproduce. The closest blackbody-based and physical models provide the following atmosphere parameters: a temperature $T = 2460^{+80}_{-160}$ K; a very low Bond albedo $A_B = 0.000^{+0.081}_{-0.000}$; and an energy redistribution parameter $P_n = 0.1$, indicating a small but nonzero amount of heat transfer from the day to nightside. The best physical model suggests a thermal inversion layer with an extra optical absorber of opacity $\kappa_e = 0.05$ cm^2 g^{-1}, placed near the 0.1 bar atmospheric pressure level. This inversion layer is located 10 times deeper in the atmosphere than the absorbers used in models to fit mid-infrared *Spitzer* detections of other irradiated hot Jupiters.

Key words: binaries: eclipsing – planetary systems – stars: individual (CoRoT-1) – techniques: photometric

Online-only material: color figures, machine-readable table

1. INTRODUCTION

Space-based detections of hot Jupiter atmospheres have flourished in recent years. The *Spitzer Space Telescope* has successfully detected thermal emission from several planets at wavelengths longer than 3.6 μm (e.g., Charbonneau et al. 2005; Deming et al. 2005, 2007; Knutson et al. 2007, 2008; Harrington et al. 2007; Machalek et al. 2008, 2009), while near-infrared (1.5–2.5 μm) observations with the *Hubble Space Telescope* have found evidence for water, carbon monoxide, and carbon dioxide in the dayside spectrum of the exoplanet HD 189733b (Swain et al. 2009). These detections have been made during secondary eclipses (when the planets pass behind their host stars). Important atmospheric absorption signatures have been detected by transit observations with these space telescopes as well: sodium in HD 209458b (Charbonneau et al. 2002) and methane in HD 189733b (Swain et al. 2008) with *Hubble*, and water vapor in HD 189733b with *Spitzer* (Tinetti et al. 2007).

The *CoRoT* mission recently joined these space-borne successes by detecting phase brightness variations and combined thermal and reflected emission during secondary eclipses of the exoplanets CoRoT-1b (Snellen et al. 2009; Alonso et al. 2009) and CoRoT-2b (Alonso et al. 2009) in an optical broadband window centered at about 0.6 μm (see Table 1).

At the same time that these detections have provided very valuable insights into the atmospheric physics of irradiated hot Jupiters, they have also revealed some perplexing findings. Some of the planets show a strong temperature contrast between their day and nightsides (e.g., Harrington et al. 2006; Snellen et al. 2009), while others appear to have a more efficient redistribution of incident energy (e.g., Knutson et al. 2007). Another striking discovery is an apparent bifurcation of hot Jupiters into two classes based on the presence or absence of a thermal inversion layer (e.g., Hubeny et al. 2003; Burrows et al. 2008b; Fortney et al. 2008). Along with a wider than expected range of exoplanet radii (see e.g., Barge et al. 2008), these are currently the key unsolved questions in the study of irradiated hot Jupiter atmospheres.

Resolving these questions will require observations from the optical to the infrared wavelength regimes. Ground-based observations have just recently started to reach the sensitivity necessary to directly detect hot Jupiters. The first two detections were announced in early 2009 at optical and near-infrared wavelengths: OGLE–TR–56b in z'-band (Sing & López-Morales 2009), and TrES-3 in K band (de Mooij & Snellen 2009). The third ground-based result was the detection of an eclipse of CoRoT-1b at 2.09 μm (Gillon et al. 2009). This last detection makes CoRoT-1b the first exoplanet to have thermal emission measured at both optical and near-infrared wavelengths.

Here, we report the fourth ground-based detection of thermal emission from an exoplanet, and the fourth detection of CoRoT-1b, this time in Ks-band (2.15 μm). We combine our results with the other three recent detections of CoRoT-1b by Snellen et al. (2009), Gillon et al. (2009), and Alonso et al. (2009) to produce the first multi-color analysis of the atmospheric spectrum of an exoplanet between 0.5 and 2.2 μm.

---

* Based on observations obtained with the Apache Point Observatory 3.5 m telescope, which is owned and operated by the Astrophysical Research Consortium.
[6] Hubble Fellow.

Table 1
Transmission Information of Each Detection Filter, Along with the Planet-to-star Flux Ratio and Physical Flux Density of the Planet in Each Filter

Filter	λ_{eff} (μm)	FWHM (μm)	Peak Trans. (%)	Planet: Star Flux Ratio (%)	Physical Flux Density (Jy)
CoRoT white	0.60	0.42	72	0.016 ± 0.006[a]	0.0093 ± 0.0035
CoRoT red	0.71	0.25	72	0.0126 ± 0.0033[b]	0.0081 ± 0.0023
NB 2090	2.095	0.020	82	$0.278^{+0.043}_{-0.066}$[c]	$0.1094^{+0.0169}_{-0.0260}$
Ks	2.147	0.318	97.5	0.336 ± 0.042[d]	0.1172 ± 0.0160

Note. The physical flux densities are calculated for a hypothetical distance of 10 pc.
References. (a) Alonso et al. 2009; (b) Snellen et al. 2009; (c) Gillon et al. 2009; (d) This work.

Section 2 describes the observations. In Section 3, we detail our reduction and analysis steps to detect the signal from the planet. Section 4 compares the detected signals to the predictions made by state-of-the-art planetary atmosphere models. The results are then discussed and summarized in Sections 5 and 6.

2. OBSERVATIONS

We observed two secondary eclipse events of CoRoT-1b on the nights of 2009 January 9 and 15, UT, using the Near-Infrared Camera & Fabry–Perot Spectrometer (NICFPS) on the ARC 3.5 m telescope at Apache Point Observatory in New Mexico. Windy conditions and thin and constantly varying cirrus layers hampered our attempts to reach high-precision photometry in the January 9 observations. The conditions on January 15 produced good quality data, which we will discuss here.

NICFPS is equipped with a Rockwell Hawaii 1-RG 1k×1k HgCdTe detector with a 4.58×4.58 arcmin field of view and a pixel scale of 0.273 arcsec pixel^{-1}. We chose the reddest available broadband filter (*Ks*) in order to maximize the eclipse depth and collected a large number of photons in as short an exposure time as possible. The instrument has a high read noise (95 e^- pixel^{-1}), which can be reduced through the use of up to 15 Fowler samples. In this mode, the chip is read out non-destructively a number of times during the exposure, and the difference of each pair of readouts is taken as one sample.

We used the instrument in the standard eight Fowler sample mode, in which the chip is read out 16 times consecutively while exposing. The first readout is subtracted from the ninth, the second from the tenth, and so forth, producing eight 5.44 s samples in 10.88 s. We then use the average of the eight resulting differences, which reduces the read noise of the detector to 35 e^- pixel^{-1} (a factor of $\sqrt{8}$). To achieve a good sky subtraction, we used a simple two-point dither pattern, taking a set of two exposures and then offsetting the objects by 58 pixels (15.8 arcsec). This resulted in two exposures every ~50 s, when combining the exposure, readout, and offset times. With a measured gain of 4.77 e^- ADU^{-1}, we collected ~782,000 photons per data point from the target, and 746,000 to 1,417,000 photons per data point from the nearby comparison stars. Based on the noise expression derived by Howell (1989) to combine the Poisson noise with the sky level, dark current, and read noise, we expected the noise per data point to be 0.259%.

In order to capture the full secondary eclipse and a good baseline for the light curve, we monitored the target from 04:20 to 09:40 UT (twice the eclipse's duration), obtaining 758 frames over the course of 5.3 hours. While the transparency was excellent, the seeing varied between 0.97 and 1.91 arcsec. Throughout the observations, slow drifts in telescope pointing led to a varying target location within a ~4 pixel circle.

In addition to the target observations, we took 120 dome flats with dim quartz lamps in the *Ks* filter, and 400 dark frames, each for a range of exposure times from 1 to 8 s.

3. REDUCTION AND ANALYSIS

We began the data reduction by subtracting from each dome flat the average of the dark frames for the flat's exposure time, and then combining all the flats to create one master normalized flat. We then applied the flat-field correction to the target images, and created reduced, sky-subtracted images by subtracting from each image the nearest neighbor frame taken at the opposite dither position.

Two team members then performed independent analyses of the data, as discussed in Sections 3.1 and 3.2, in order to minimize systematics and achieve the optimal photometry. In both analyses, we converted the JD in the headers of the images to HJD and then to an orbital phase using the most recent ephemerides for transits of CoRoT-1b by Bean (2009).

3.1. Analysis A

The first approach analyzed the combined dither positions as a single data set. Several stars, including the target, were isolated enough in the frames to be analyzed by standard aperture photometry.

Using the IDL adaptation of DAOPHOT, we recorded the flux from CoRoT-1, plus another 20 bright, isolated stars in the field, for aperture sizes from 1 to 20 pixels, in increments of 0.05 pixels. Of the 20 field stars, we selected as comparisons the four that produced the most stable flux ratios with respect to the target, i.e., the differential light curves with the least photometric dispersion during the predicted out-of-eclipse phases. The locations of these four best comparisons are shown along with the target in Figure 1. A fixed aperture size of 6.1 pixels (1.67 arcsec) and a 14–24 pixel (3.82–6.55 arcsec) sky annulus produced the most stable differential photometry when combining the curves from all four comparisons. The average photometric dispersion in the out-of-eclipse portion of the combined light curve was 0.781%, a factor of 3.02 larger than the expected noise per data point.

However, the combined curve also showed clear systematic trends that could be attributed to atmospheric effects such as seeing and air mass, as well as instrumental effects such as changes in the (x, y) position of the stars in the images or temperature and pressure changes in the instrument throughout the duration of the observations.

These trends were individually investigated by fitting a linear correlation between each parameter and the differential flux, for the out-of-eclipse points only. The most significant systematic trends correlated with variations in the seeing, and we found that nearly all the systematic noise in the light curves vanished after removing a trend based on that parameter.

For the final photometry we detrended each differential light curve with respect to seeing, and then combined the four, ending up with a dispersion of 0.547%, 2.11 times the expected noise limit. The final light curve from this analysis is shown in the top panel of Figure 2.
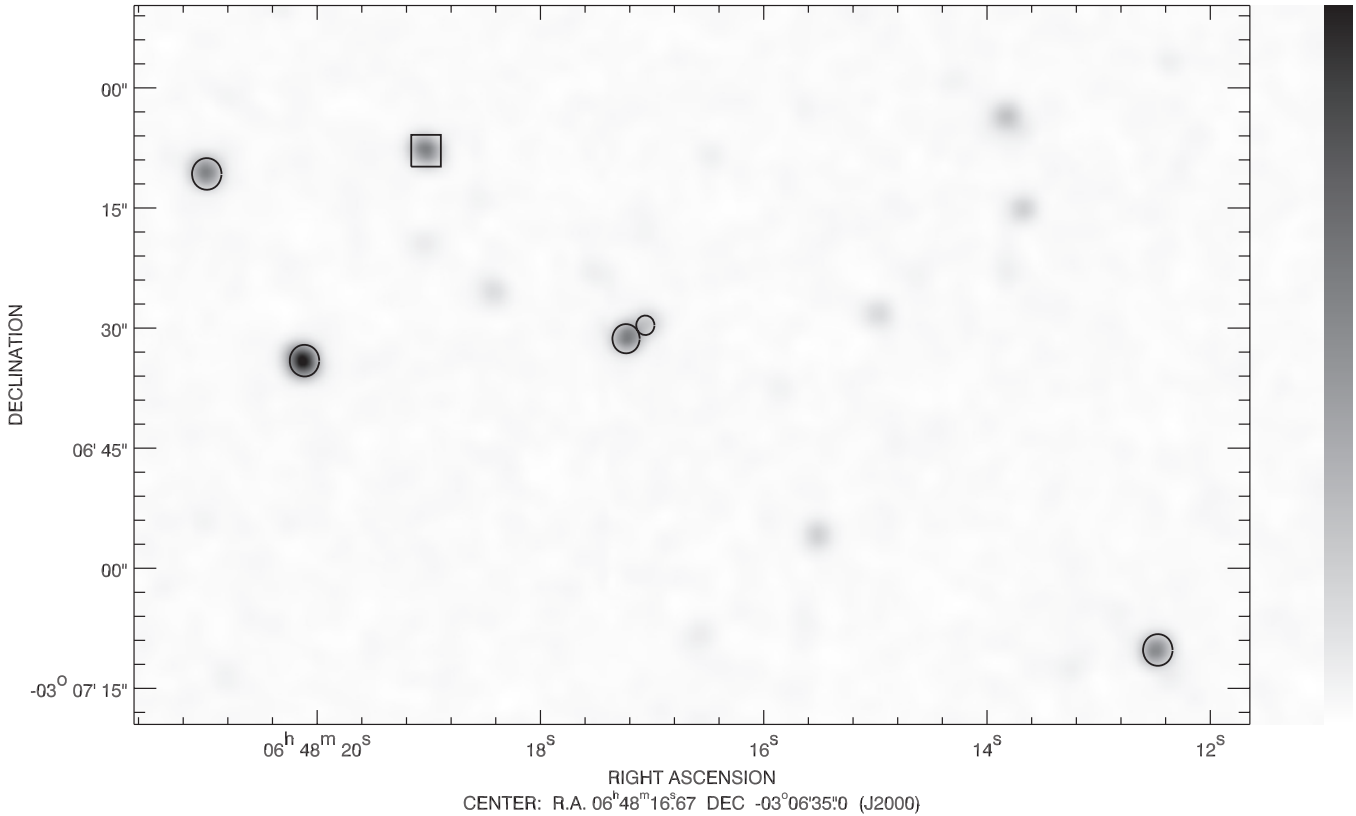
Figure 1. Finder chart for CoRoT-1 target (enclosed in square) and the field stars selected as photometric comparisons. The four stars used in analysis A are enclosed in the larger circles, while analysis B used those four plus the star in the smaller circle.

3.2. Analysis B

The second analysis approach, analogous to that of Sing & López-Morales (2009), began with the separation of the two dither position sets into different light curves, and implemented the SysRem algorithm (Tamuz et al. 2005) for de-correlation.

We used standard IDL procedures to perform aperture photometry on 19 stars, including the target, for aperture sizes between 1.0 and 14.9 pixels spaced in increments of 0.1 pixel. The centers of each star were determined by fitting a two-dimensional moffat function to the point-spread function (PSF) of each star. The residual sky background was determined by finding the sky annulus which resulted in the highest target signal-to-noise ratio (photometry error with photon, sky, and read noise). On the basis of this evaluation, the best sky annulus resulted to be one of inner radius 19 pixels and outer radius 20 pixels, corresponding to 120 pixels between 5.19 and 5.46 arcsec from the star.

The five stars selected as comparisons in this analysis are shown in Figure 1. The comparison selection criterium was the same as in analysis A, i.e., the field stars that produced the most stable photometry with respect to the target during the out-of-eclipse phase. Later comparison showed that the four reference stars used in analysis A overlap with these five.

After producing individual light curves for each dither position, we de-correlated the curves using an implementation of the SysRem algorithm (Tamuz et al. 2005), which seeks to minimize the expression

$$\sum (r_{ij} - c_i a_j)^2 / \sigma_{ij}^2, \tag{1}$$

where r_{ij} is the average-subtracted stellar magnitude for the *i*th star of the *j*th image, σ is the uncertainty of r_{ij}, c_i is an epoch-

dependent parameter, and a_j is a stellar-dependent parameter. The first pass through the SysRem algorithm produced a light curve with a single clear linear trend. We found this linear trend to be efficiently removed by either a second pass through the SysRem algorithm or by allowing the baseline flux to vary in time linearly, fit by two parameters. Removing this linear trend effectively removed any detectable systematic trends. We fit each dither position individually at first, but found that the linear slope was similar for both, and re-combined the sets.

In order to test the effectiveness of our de-correlation procedures, we searched for the presence of residual systematic errors correlated in time ("red noise"; Pont et al. 2006) by checking that the binned residuals followed an $N^{-1/2}$ relation, when binning in time by N points. The presence of red noise causes the variance to follow a $\sigma^2 = \sigma_w^2 / N + \sigma_r^2$ relation, where σ_w is the uncorrelated white noise component, while σ_r characterizes the red noise. We found no significant evidence for red noise when binning on time scales up to 42 minutes (100 points), showing that any correlated noise had been effectively removed by the de-trending.

The optimal aperture size of 5.6 pixels (1.53 arcsec) was determined to be that which minimized the standard deviation of the light curve when using the target and reference stars in these de-trending procedures. The final light curve from this analysis had a dispersion of 0.661%, 2.55 times the expected noise limit. The final light curve from this analysis is shown in the second panel of Figure 2.

3.3. Secondary Eclipse Fit

The next step in our analysis was to search for the eclipse signal from the planet in the observed light curves. This was
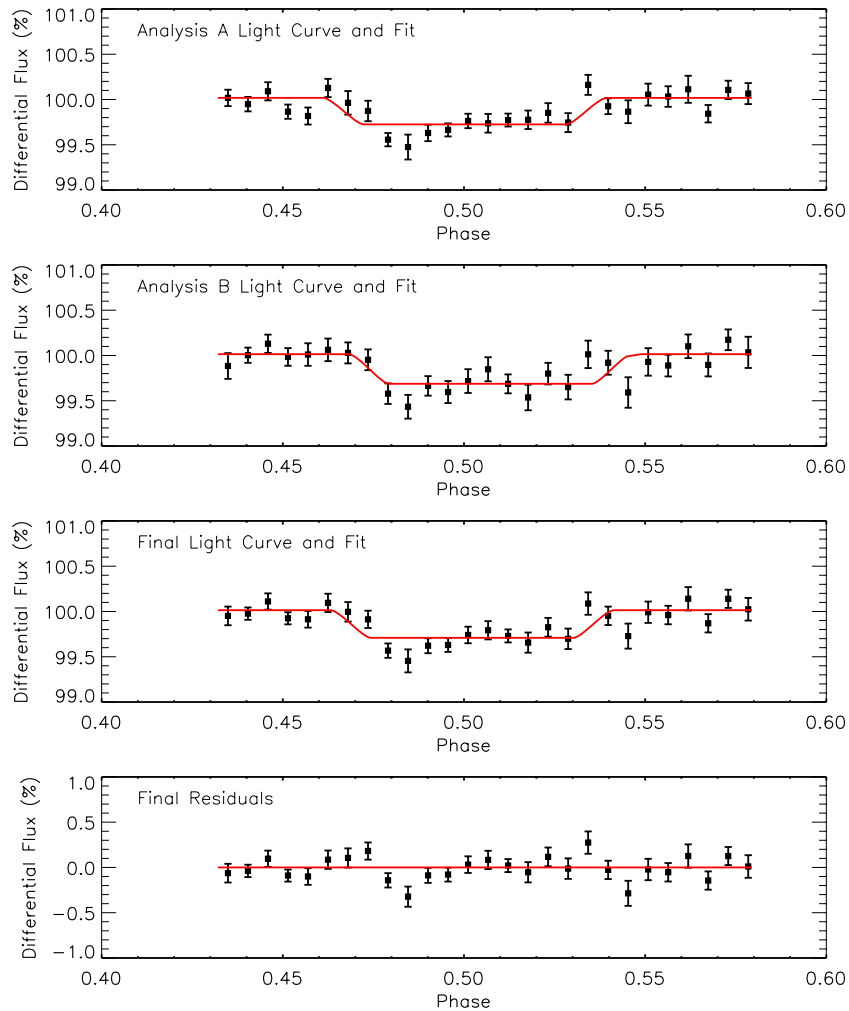
Figure 2. Top panel: light curve from analysis A after de-trending, with its best-fit model. Second panel: light curve and best-fit model from analysis B after de-trending and removal of the remaining linear trend. Third panel: final light curve calculated by combining analyses A and B. A model with the best-fit secondary eclipse is shown as the horizontal red line, with best-fit central phase shift of 0.5022. The baseline is set at 100.010%, with an eclipse depth of 0.336%. Bottom panel: flux residuals (observed model) for the combined light curve. In all plots, each point corresponds to a 12 minute bin.

(A color version of this figure is available in the online journal.)

Table 2
Final Light Curve, Calculated by Averaging the Point-by-point Average of the Results from Analyses A and B

HJD	Orbital Phase	Observed Flux	Flux Error
2454846.686842	0.4320984781	0.9939594865	0.0052779813
2454846.687166	0.4322515726	1.0044958591	0.0052779813
2454846.687398	0.4324662685	1.0090936422	0.0052779813
2454846.687722	0.4326120615	0.9946241379	0.0052779813
2454846.687942	0.4328347445	1.0004521608	0.0052779813

(This table is available in its entirety in a machine-readable form in the online journal. A portion is shown here for guidance regarding its form and content.)

done separately for each light curve resulting from analyses A and B, and the solutions were then combined to produce a final result.

We used the orbital period from Bean (2009) and the stellar and planetary radius from Gillon et al. (2009; see Table 3) to generate a grid of eclipse models with no limb darkening and a constant out-of-eclipse baseline. The free parameters in the model grid were the baseline level and the depth and central phase of the eclipse, with the grid covering baseline levels between 99.6% and 100.4% in increments of 0.002%, eclipse

depths between 0 and 0.8% in 0.002% steps, and central phases between 0.46 and 0.54 in 0.0001 phase increment steps. Running each light curve through the model grid resulted in the following best-fit solutions: for the analysis A light curve, a baseline of 100.014% and an eclipse of depth 0.322%, centered at phase 0.5003; for the analysis B light curve, a baseline of 100.006%, an eclipse depth of 0.355%, and a central phase of 0.5073. We decided to use the point-by-point average of the light curves from analyses A and B for our final result, shown in the third panel of Figure 2. Table 2 shows the first few unbinned points in the final result, and the full data set is available in the online version. The best fitting model in that case, found via chi-square minimization and with a reduced χ^2 of 1.051, gave a baseline of $100.010^{+0.042}_{-0.040}$ %, an eclipse depth of $0.336^{+0.068}_{-0.064}$ and a central phase $0.5022^{+0.0023}_{-0.0027}$. These values are given, along with the other parameters of the system, in Table 3. The results of each fit for the entire parameter space are shown in Figure 3.

To estimate the error in the eclipse depth, we put all the in-eclipse points from the de-trended photometry into a single bin, the entire out-of-eclipse portion into a second bin, and combined the binned errors. We had 295 in-eclipse points with an average individual dispersion of 0.531%, and 344 out-of-eclipse points with an average individual dis-
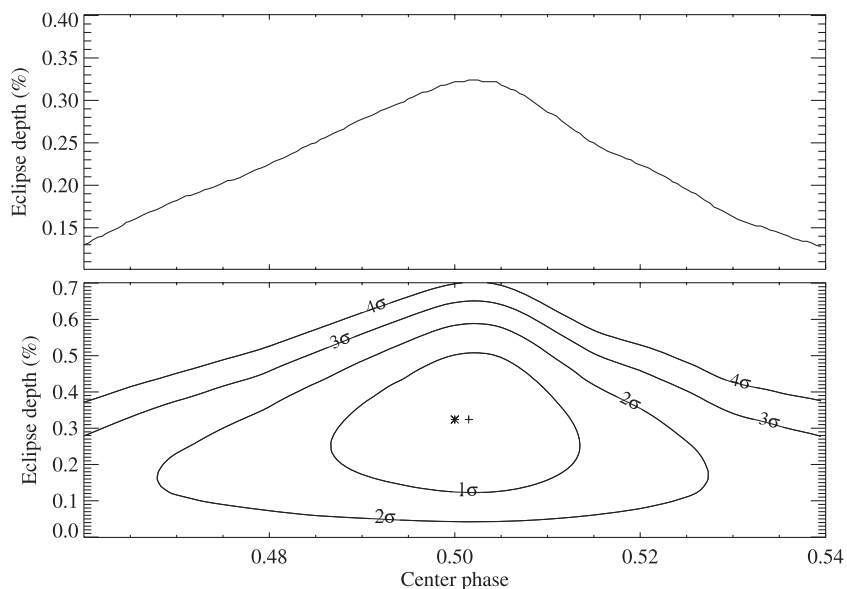
Figure 3. Top panel: model eclipse depth vs. central phase for phases between phases 0.46 and 0.54. The best model fit to the data has a depth of 0.336% and central phase 0.5022. The eclipse depth falls rapidly in both directions away from that phase value. Bottom panel: confidence contours of the best fit at the 68.3%, 95.5%, and 99.7% level. The best-fit value is indicated as a cross at phase 0.5022. The star at 0.5 indicates the phase of the expected center of the eclipse for a circular orbit. The result is therefore consistent with a zero eccentricity orbit ($e \cos \omega = 0.0035^{+0.0036}_{-0.0042}$).
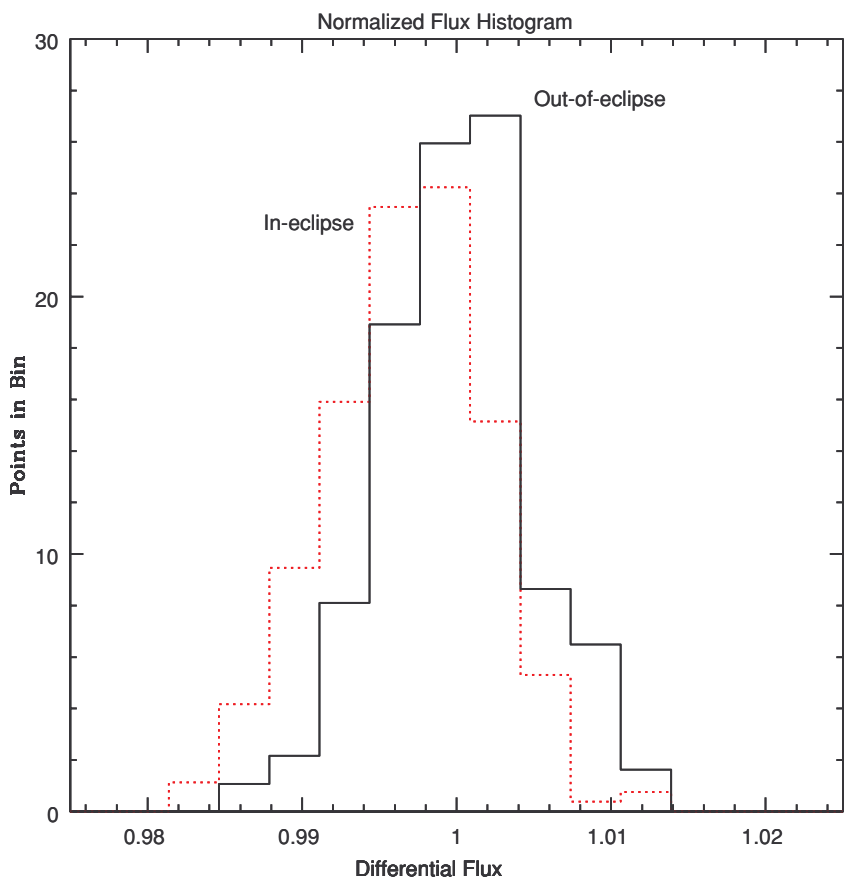

Figure 4. Normalized flux histograms of the in-eclipse (red dotted line) and out-of-eclipse (black solid line) portions of the CoRoT-1b light curve in Figure 2. The width of each bin is 0.336%, the same as the detected eclipse depth.

(A color version of this figure is available in the online journal.)

persion of 0.528%, which combined to give us a 1σ error of 0.042%. For the error in phase we have directly adopted the 1σ confidence values from the contour plot in Figure 3.

As an additional test to confirm the depth of the eclipse, we generated histograms of the distribution of normalized flux for both the in-eclipse and out-of-eclipse portions of the light curve, adopting as central eclipse phase the value $\psi = 0.5022$ obtained
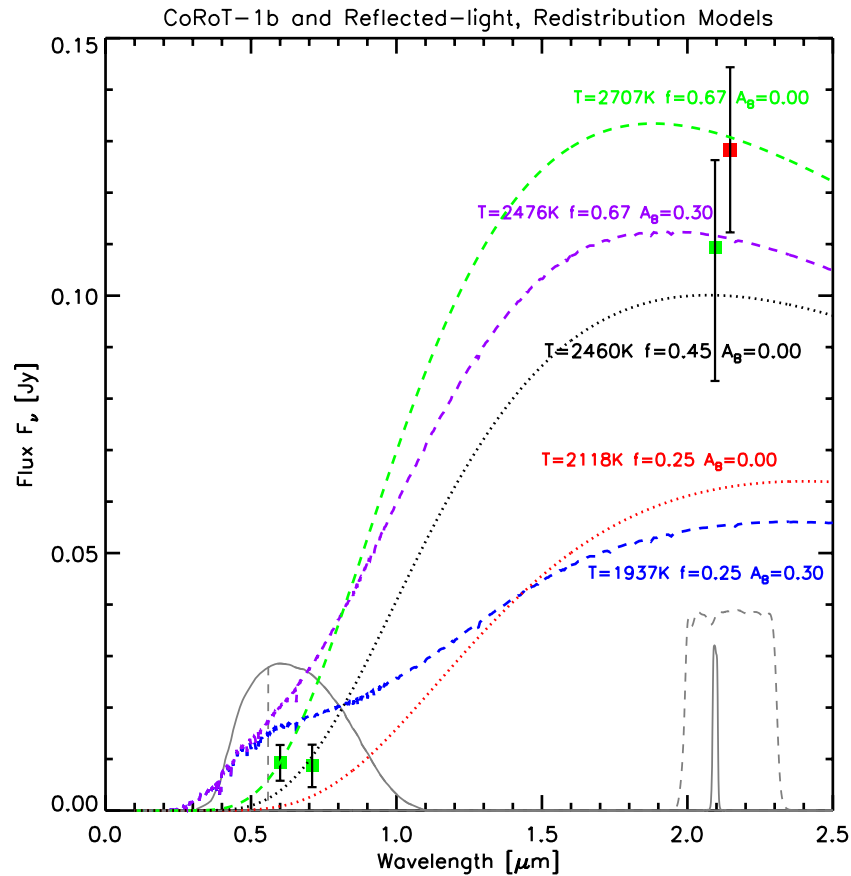
Figure 5. Comparison of the four detected CoRoT-1b planet fluxes with models that include reflected light and heat redistribution, for a range of Bond albedo (A_B) and re-radiation factors (f). We show two models with maximum energy redistribution ($f = 1/4$) and Bond albedos of 0 (red) and 0.3 (blue), and two models with no energy redistribution ($f = 2/3$) and Bond albedos of 0 (green) and 0.3 (purple). The best-fit model, shown in black, is for a zero-albedo planet with a small, but non-zero amount of heat redistribution. At the bottom of the figure, we show scaled transmission functions for each of the filters used: *CoRoT* (the dashed line shows the blue cutoff for the red channel), NB2090 (solid), and *Ks* (dashed).

above. The result, shown in Figure 4, shows a clear 0.336% shift of the distribution of in-eclipse points with respect to the out-of-eclipse points, in full agreement with the result of the model grid fits.

4. ATMOSPHERE MODEL FITS

While secondary eclipse detections in a single broadband, such as the optical detections with the *CoRoT* data (Snellen et al. 2009; Alonso et al. 2009), cannot constrain a planet's thermal and reflected light independently of one another, we can begin to disentangle the reflected and thermal contributions to the total light from the planet by comparing the secondary eclipse depths at different wavelengths. Combining our *Ks*-band eclipse detection of CoRoT-1b with the other three detections by Snellen et al. (2009), Gillon et al. (2009), and Alonso et al. (2009), in this section we make the first simultaneous multi-wavelength comparison of observations of an exoplanet atmosphere to current models at optical and near-infrared wavelengths.

In the following subsections, we compare the observations first to simple blackbody models and then to more sophisticated radiative–convective models of irradiated planetary atmospheres in chemical equilibrium. The advantage of the blackbody models is that they provide simple initial estimates of the global properties of the planetary atmospheres, such as their approximate temperatures, their reflective properties, and how efficiently they redistribute energy from the irradiated to the

non-irradiated sides (see, e.g., López-Morales & Seager 2007). Atmosphere models provide more details about specific properties of the atmospheres, such as finer spectral information. This allows the identification of specific absorbing or emitting chemicals, as well as their specific atmospheric depths, and the presence of thermal inversion layers (see, e.g., Burrows et al. 2008a).

4.1. From Contrasts to Flux Densities

Before beginning the model comparisons, we converted the measured eclipse depths to planetary fluxes, because secondary eclipse photometry does not provide an absolute measure of the planet's brightness, but a planet-to-star flux ratio integrated through the instrument and filter profile.

For this conversion, we calculated the synthetic flux density of a Kurucz (1993) G0V-type star, equivalent to the CoRoT-1b host star, in the *CoRoT* White, *CoRoT* Red, NB2090, and *Ks* filters using each filter's response curve. The *CoRoT* White, NB2090, and *Ks* filters have well-defined transmission functions centered at 0.6, 2.09, and 2.15 μm, respectively, but the response curve for the *CoRoT* Red channel is not as well known. The collected light is passed through a prism that divides it into red, green, and blue portions, but the behavior is different for each star. Following Snellen et al. (2009), we estimated a wavelength cutoff of ∼560 nm by taking the fraction of light in the red channel to the total light, giving an effective wavelength of
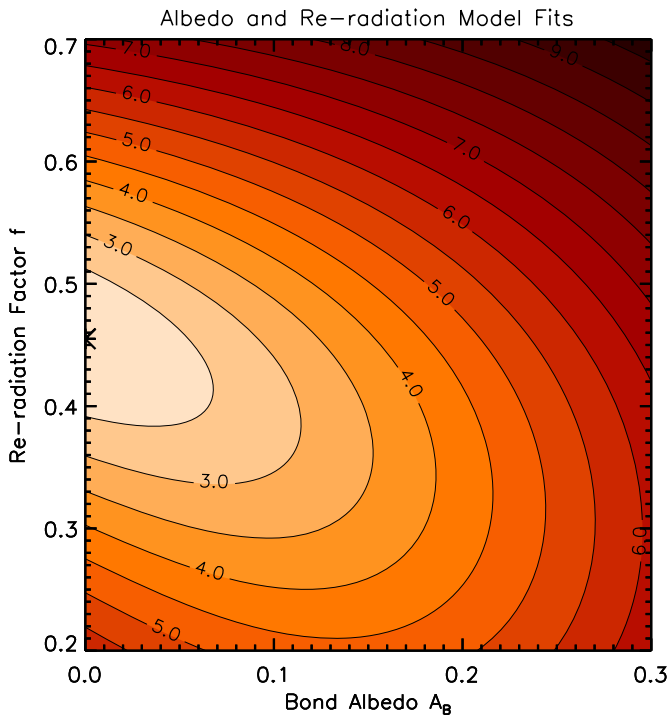
Figure 6. Contour plot showing the best-fit albedo and re-radiation factors for the planet fluxes detected. The contour levels show the total four-dimensional distance of each model from the observations, expressed in units of uncertainties. This was calculated by summing the squares of the differences between the observed and predicted flux densities divided by the uncertainty at each wavelength, and taking the sum's square root, i.e., equivalent to the square root of the χ^2 value. The data clearly favor a very low-albedo planet with inefficient but measurable energy redistribution, with the best fit (indicated by a bold X) at $A_B = 0.000^{+0.081}_{-0.000}$, $f = 0.450^{+0.065}_{-0.085}$, producing a temperature of 2460^{+80}_{-160} K.

710 nm. To approximate the behavior of the red channel, we used the same response curve as for the white channel, but with zero transmission below 560 nm.

For the purposes of the comparison, we used a hypothetical distance of 10 pc (i.e., the physical flux density of the star and planet were derived for this standard scale distance, not their actual distance). We then multiplied each synthetic stellar flux density by the observed planet-to-star contrast in that band. The resulting planet flux densities are summarized in Table 1, together with the observed contrasts and the parameters of each filter. The derived planet flux densities are also shown in Figure 5.

We note that the contrasts observed and the flux densities calculated for CoRoT-1b in the NB2090 and the Ks filters are very similar, our measurement confirming the detection made by Gillon et al. (2009).

4.2. Blackbody-based Planet Models

In the blackbody approximation, the temperature profile of an irradiated planet will be a smooth combination of reflected and thermally emitted light. That temperature profile is determined by the interplay of the stellar irradiation, Bond albedo A_B, and a re-radiation factor f, which describes how efficiently energy from incident radiation is transported around the planet before being re-emitted. Following López-Morales & Seager (2007), the value $f = 2/3$ corresponds to no redistribution before re-radiation and $f = 1/4$ corresponds to the incident energy being evenly redistributed around the planet. The combination of the optical and near-infrared measurements of CoRoT-1b

provide powerful constraints on both the reflected light (i.e., planetary albedo) and the heat redistribution between the day and nightsides of the planet. In this section, we apply models combining reflected light and thermal blackbody radiation to interpret the detections. The results are illustrated in Figures 5 and 6.

Figure 5 includes the four measured planetary flux densities, normalized to a distance of 10 pc, along with models with different temperature, albedo and re-radiation factor values. The effect of increasing the albedo is to increase the flux density measured in the optical (which corresponds to reflected light), while decreasing the infrared emission due to the lower absorbed energy. Increasing the day to nightsides heat redistribution lowers the entire spectral energy distribution, but does not shift the balance between the optical and near-infrared flux densities. The models shown in the figure reveal that the observations are entirely inconsistent with efficient day–night heat redistribution and also exclude a high albedo.

Figure 6 shows the result of exploring the entire A_B–f parameter space using the observed flux densities and the thermal emission plus reflected light models. To quantify the constraints and identify the best fit, we evaluated these models along a grid spanned by Bond albedos $A_B = 0$–0.3 and re-radiation factors $f = 1/4$–$2/3$, calculating at each grid point the predicted temperature, the predicted flux densities in the four observed bands, and a χ^2 value. The contour levels in the figure show the total four-dimensional distance of each model from the observations, expressed in units of uncertainties. This was calculated by summing the squares of the differences between the observed and predicted flux densities divided by the uncertainty at each wavelength, and taking the sum's square root, i.e., equivalent to the square root of the χ^2 value. The best fit corresponds to a model with dayside temperature 2460^{+80}_{-160} K, a very low albedo ($A_B = 0.000^{+0.081}_{-0.000}$), and inefficient but measurable heat redistribution ($f = 0.450^{+0.065}_{-0.085}$). These parameters are given in the third section of Table 3. Thus, our simple blackbody-based modeling suggests a low-albedo planet with some measurable levels of energy re-distribution, but still a very prominent temperature difference between the day and nightsides.

4.3. Theoretical Atmosphere Models

Due to prominent molecular absorption bands heavily irradiated giant planet atmospheres are thought to display an emission spectrum very unlike a blackbody. Thus, while the blackbody models provide useful first estimates of the planetary properties, realistic atmospheric models are required to derive the actual physical properties of the planets. To gain more detailed information about the physical and chemical processes undergoing in the atmosphere of CoRoT-1b, we compared the observations to the latest, and still evolving, models of irradiated hot Jupiter atmospheres.

The model atmospheres we used are derived from self-consistent coupled radiative transfer and chemical equilibrium calculations, based on the models described in Sudarsky et al. (2000, 2003), Hubeny et al. (2003), and Burrows et al. (2005, 2006, 2008a). The most important components of the code include molecular and atomic opacities, and calculations to determine the chemical abundances using thermochemical models (e.g., Sharp & Burrows 2007). The day and nightsides of the planet are treated separately, with the dayside receiving incident flux from the star using the appropriate Kurucz (1993) spectral model, and the nightside receiving heat from the dayside via

Table 3
Star and Planet Parameters

Parameter	Value	Unit	Reference
Stellar Parameter			
Apparent K magnitude	12.15		1
Stellar mass, $M_\star$	$1.01^{+0.13}_{-0.22}$	$M_\odot$	3
Stellar radius, $R_\star$	$1.057^{+0.055}_{-0.094}$	$R_\odot$	3
Star, $T_{\rm eff}$	5950 ± 150	K	1
log g	4.25 ± 0.30	(cgs)	1
$[M/H]$	-0.3 ± 0.25	dex	1
R.A. (J2000)	06 48 19		1
Decl. (J2000)	$-03\ 06\ 08$		1
Measured Planet Parameter			
Planet mass, M_p	$1.07^{+0.13}_{-0.18}$	M_J	3
Planet radius, R_p	$1.45^{+0.07}_{-0.13}$	R_J	3
Transit epoch, T_0	$2454159.452879 \pm 0.000068$	HJD	2
Orbital period	$1.5089686^{+0.0000005}_{-0.0000006}$	days	2
Semimajor axis, a	$0.0259^{+0.0011}_{-0.0020}$	AU	3
Orbital inclination, i	$85.66^{+0.62}_{-0.48}$	degrees	3
Mid-eclipse phase	$0.5022^{+0.0023}_{-0.0027}$		4
Orbital eccentricity $e\cos\omega$	$0.0035^{+0.0036}_{-0.0042}$		4
2.2 μm eclipse depth	$0.336 \pm 0.042\%$		4
Blackbody Model-derived Planet Parameter			
Bond albedo, A_B	$0.000^{+0.081}_{-0.000}$		4
Re-radiation factor, f	$0.450^{+0.065}_{-0.085}$		4
Blackbody model temperature, T_{bb}	2460^{+80}_{-160}	K	4
Physical Model-derived Planet Parameter			
Bond albedo, A_B	0.075 ± 0.015		4
Energy redistribution factor, P_n	0.1		4
Absorber opacity, κ_e	0.05	cm^{2}g^{-1}	4
Absorber depth in atmosphere	0.1	bar	4
Temperature at absorber depth	2200	K	4

References. (1) Barge et al. 2008, (2) Bean 2009, (3) Gillon et al. 2009, (4) This work.

convection. The convection is modeled with a mixing length equal to the pressure scale height (Burrows et al. 2008a). The heat redistribution, described by a parameter P_n, is used to derive the planet's flux at the time of secondary eclipse (Burrows et al. 2008b). The P_n parameter represents the fraction of the incident stellar energy that is redistributed to the nightside ($P_n = 0$ corresponds to no redistribution; $P_n = 0.5$ is uniform distribution around the planet).[7]

The immediate conclusion from applying the base models described above is that atmospheres with no thermal inversion, unable to reproduce the near-infrared fluxes we observe, can be confidently excluded. Therefore, we modified those models by adding an extra optical (0.37–1.0 μm) absorber with a constant opacity κ_e to the abundances predicted by the chemical equilibrium calculations. This absorber, placed at an atmospheric height (i.e., pressure) of $P = 0.01$ bar, has the effect of creating a strong temperature inversion, with the extra optical absorption heating the stratosphere. Some of the resulting representative models are shown in Figure 7.

The upper panel in the figure shows identically irradiated planets, but with different redistribution parameters ($P_n = 0.1$, 0.3, 0.5) and extra absorber opacities ($\kappa_e = 0.0$, 0.1, 0.0 cm^2 g^{-1}). Models with no energy redistribution (i.e., $P_n = 0.0$) were

too bright in the optical regime to fit the two *CoRoT* points. Although representing diverse planetary atmospheres, none of these three, nor any of the other models, reproduced the observed very bright near-infrared flux densities.

In an attempt to more closely reproduce the high observed near-infrared fluxes, we used an atmosphere model with $P_n = 0.1$ and $\kappa_e = 0.05$ cm^2 g^{-1}. The extra absorber had to be placed deeper in the atmosphere (at $\sim$0.1 bar). This is a factor of 10–100 deeper than what has been used to fit the *Spitzer* data for other hot Jupiters, in which case an extra optical absorber at $\sim$$10^{-3}$–$10^{-2}$ bar reproduced the IRAC points (e.g., Machalek et al. 2008). The temperature at this layer, also calculated by the model, is around 2200 K. The result of this final model attempt is illustrated in the lower panel of Figure 7. This model fits the NB2090 and *CoRoT* channel observations fairly well (within 0.9σ), but still underpredicts the observed *Ks*-band flux density by 2.6σ. Still, there is some improvement over the upper-panel models, for which the *Ks*-band deviations are between 3.3 and 4.9σ. The parameters in this best-fit model are also listed in Table 3.

Previous to this work, there were virtually no observational constraints on hot Jupiters in this wavelength range. Although a perfect model match to the near-infrared data has yet to be achieved, the results reveal very hot temperatures at low–to–moderate optical depths, i.e., in the upper stratospheres probed by the 2-micron observations (e.g., Figure 1 in Burrows et al. 2008a).

---

[7] $P_n = 0$ (no energy redistribution) corresponds to $f = 2/3$ and $P_n = 0.5$ (maximum redistribution) corresponds to $f = 1/4$. However, as the physical models incorporate factors that are accounted for differently than in the blackbody models (e.g., pressure, opacity), the P_n–f relation is degenerate, i.e., multiple P_n values may correspond to the same f value.
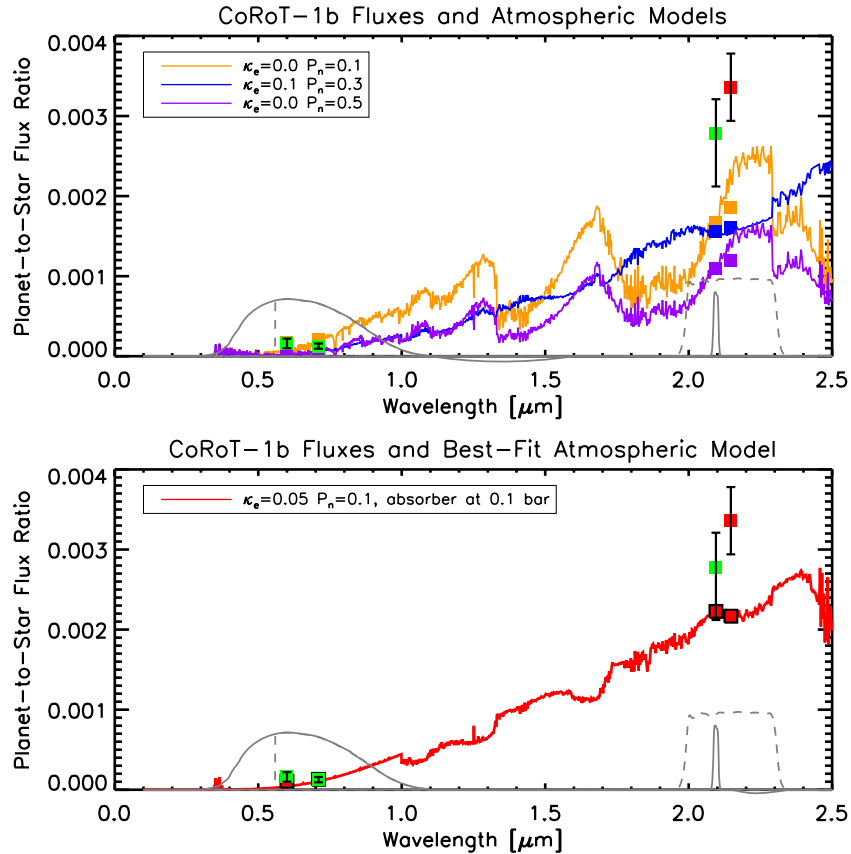
Figure 7. Top panel: the measured planet-to-star flux ratios compared to the band-averaged ratios from atmospheric models that incorporate extra optical absorbers placed near the 0.01 bar level. Three models shown here in orange, blue, and purple, have absorber opacities κ_e = 0.0, 0.1, and 0.0 cm^2 g^{-1}, and redistribution parameters P_n = 0.1, 0.3, and 0.5, respectively. Bottom panel: the measured flux ratios compared to the predicted ratios from the best-fit atmospheric model, with κ = 0.05 cm^2 g^{-1} and P_n = 0.1, and the absorber placed near the 0.1 bar level, deeper in the atmosphere than for the other models.

5. DISCUSSION

The detections of exoplanets via transits and secondary eclipses have produced many of the most valuable insights to their physical properties, but also yielded some puzzling results. Among these is the apparent division of the population of hot Jupiters into two distinct classes based on their atmospheric properties: one group that appears cooler, with water and methane absorption bands and more efficient energy redistribution, and another with higher levels of thermal emission, strong day–night contrasts, and lacking the expected absorption bands. The dominant explanation for this dichotomy is the presence in many planets of a thermal inversion layer, i.e., a hot stratosphere caused by extra absorbers of optical light (Hubeny et al. 2003; Burrows et al. 2008b; Fortney et al. 2008).

The exact nature of the absorbers is a difficult question still being investigated. Spiegel et al. (2009) recently argued that vanadium oxide is not likely to fulfill this role, and that the previously favored titanium oxide would require unusually high levels of macroscopic mixing to remain in the upper atmosphere. S$_2$, S$_3$, and HS compounds, as absorbers of optical and ultraviolet light, have also recently been both considered and questioned as causes of the thermal inversion (Zahnle et al. 2009a, 2009b). Consistent modeling of the infrared secondary eclipse spectra of six planets by Burrows et al. (2008a) suggest that the presence of the necessary absorber may depend not only on the incident stellar radiation, but also on planetary metallicity and surface gravity.

From the combination of the four optical to near-infrared detections we have detailed in this paper, it appears that CoRoT-1b clearly falls into the class of hot Jupiters with a thermal inversion. The best-fit physical model to the combined data set requires a small redistribution parameter P_n = 0.1 and an extra optical absorber with flat opacity κ = 0.05 cm^2 g^{-1}. While we cannot determine the identity of this absorber, the model constrains its altitude, requiring absorption a factor of 10–100 times deeper in the atmosphere than suggested by previous results for other exoplanets. This new constraint also highlights the power of combined optical and near-infrared photometry.

CoRoT-1b reflects some other surprising trends as well. Hot Jupiters tend to have very low albedos (Sudarsky et al. 2000; Rowe et al. 2006; Burrows et al. 2008b), and our findings place this planet's atmosphere in agreement with that trend. From the best-fit physical model derived in Section 4.3, we obtained an estimate of the planet's geometric albedo at the wavelengths probed by the *CoRoT* detections (0.4–1.0μm) to be A_g = 0.05 ± 0.01. Assuming a wavelength-independent Lambert sphere (see López-Morales & Seager 2007), this corresponds to a Bond albedo A_B = 0.075 ± 0.015.

CoRoT-1b is also notable for its extremely large radius (1.45 R$_{Jup}$; Gillon et al. 2009); evolutionary models for a hot Jupiter of its mass, age, and irradiation predict a radius of only 0.94–1.18 R$_{Jup}$ (Fortney et al. 2007). This places it toward the upper end of the wide distribution of

radii that has been seen among the population of transiting exoplanets.

While small-radius planets can be modeled with a larger, denser core, the inflated sizes of planets like CoRoT-1b provide quite a challenge to planetary models. Several explanations have been proposed, including heat retained by enhanced atmospheric opacities (Burrows et al. 2007), deposition of kinetic wind energy in the upper atmosphere (Showman et al. 2008), and significant tidal heating caused by orbital eccentricity or a rapidly rotating star (Bodenheimer et al. 2003; Greenberg 2009; Marley et al. 2009; Ibgui & Burrows 2009). Though Gillon et al. (2009) measured an eccentricity $e = 0.071^{+0.042}_{-0.028}$ for CoRoT-1b's orbit, the eccentricity we measure ($e \cos \omega = 0.0035^{+0.0036}_{-0.0042}$) based on its mid-eclipse phase is consistent within its errors with a circular orbit. Thus, there is no evidence that tidal heating derived from a currently eccentric orbit contributes to the energy budget of CoRoT-1b, although intense heating in the recent past cannot be excluded (e.g., Miller et al. 2009). In each of the diverse models, the radius of the planet is determined by the pressure–temperature structure of the atmosphere and the balance between the energy input and output. In order to understand and improve the models, we must first constrain the energy balance by understanding the basic atmospheric properties, such as chemical abundances, pressure–temperature profiles, and energy redistribution.

With our detection in Ks joining the 0.6, 0.71, and 2.09 μm measurements, we are beginning to get a more detailed picture of the atmospheric properties of CoRoT-1b. However, there are still sizeable gaps in the observed spectrum, and even the most advanced current models have difficulty explaining the high flux levels in the 2 μm window. It is crucial to add further detections in both narrow and broadbands, in the optical and near-infrared, and a larger target sample to provide stronger constraints to the planetary atmosphere models.

6. SUMMARY

1. We directly detect thermal emission from CoRoT-1b in Ks-band, determining the planet-to-star flux ratio to be 0.336% ± 0.042%.
2. Using simple blackbody-based models, we find the best fit to be a blackbody of 2460^{+80}_{-160} K, and confidently rule out both a high albedo and efficient day–night heat redistribution.
3. Using realistic atmosphere models, we find the need for a thermal inversion layer and an extra absorber near the 0.1 bar level, deeper in the atmosphere than the *Spitzer* mid-infrared data suggested for other hot Jupiters.
4. Both the blackbody models and physical atmospheric models agree on a small but non-zero amount of heat redistribution, and a Bond albedo less than 0.09.

In short, the combined optical to near-infrared photometry of CoRoT-1b has allowed us to independently constrain the reflected light and thermal emission, and has revealed a very hot, low-albedo planet with a large day–night contrast and a prominent temperature inversion.

REFERENCES

Alonso, R., Guillot, T., Mazeh, T., Aigrain, S., Alapini, A., Barge, P., Hatzes, A., & Pont, F. 2009, A&A, 501, L23
Barge, P., et al. 2008, A&A, 482, L17
Bean, J. L. 2009, A&A, 506, 369
Bodenheimer, P., Laughlin, G., & Lin, D. N. C. 2003, ApJ, 592, 555
Burrows, A., Budaj, J., & Hubeny, I. 2008a, ApJ, 678, 1436
Burrows, A., Hubeny, I., Budaj, J., Knutson, H. A., & Charbonneau, D. 2007, ApJ, 668, L171
Burrows, A., Hubeny, I., & Sudarsky, D. 2005, ApJ, 625, L135
Burrows, A., Ibgui, L., & Hubeny, I. 2008b, ApJ, 682, 1277
Burrows, A., Sudarsky, D., & Hubeny, I. 2006, ApJ, 650, 1140
Charbonneau, D., Brown, T. M., Noyes, R. W., & Gilliland, R. L. 2002, ApJ, 568, 377
Charbonneau, D., et al. 2005, ApJ, 626, 523
Deming, D., Richardson, L. J., & Harrington, J. 2007, MNRAS, 378, 148
Deming, D., Seager, S., Richardson, L. J., & Harrington, J. 2005, Nature, 434, 740
de Mooij, E. J. W., & Snellen, I. A. G. 2009, A&A, 493, L35
Fortney, J. J., Lodders, K., Marley, M. S., & Freedman, R. S. 2008, ApJ, 678, 1419
Fortney, J. J., Marley, M. S., & Barnes, J. W. 2007, ApJ, 659, 1661
Gillon, M., et al. 2009, A&A, 506, 359
Greenberg, R. 2009, ApJ, 698, L42
Harrington, J., Hansen, B. M., Luszcz, S. H., Seager, S., Deming, D., Menou, K., Cho, J. Y.-K., & Richardson, L. J. 2006, Science, 314, 623
Harrington, J., Luszcz, S., Seager, S., Deming, D., & Richardson, L. J. 2007, Nature, 447, 691
Howell, S. B. 1989, PASP, 101, 616
Hubeny, I., Burrows, A., & Sudarsky, D. 2003, ApJ, 594, 1011
Ibgui, L., & Burrows, A. 2009, ApJ, 700, 1921
Knutson, H. A., Charbonneau, D., Allen, L. E., Burrows, A., & Megeath, S. T. 2008, ApJ, 673, 526
Knutson, H. A., et al. 2007, Nature, 447, 183
Kurucz, R. L. 1993, VizieR Online Data Catalog, 6039, 0
López-Morales, M., & Seager, S. 2007, ApJ, 667, L191
Machalek, P., McCullough, P. R., Burke, C. J., Valenti, J. A., Burrows, A., & Hora, J. L. 2008, ApJ, 684, 1427
Machalek, P., McCullough, P. R., Burrows, A., Burke, C. J., Hora, J. L., & Johns-Krull, C. M. 2009, ApJ, 701, 514
Marley, M. S., Zahnle, K., Fortney, J., Lodders, K., & Freedman, R. 2009, AAS Meeting Abstracts, 214, 306.02
Miller, N., Fortney, J. J., & Jackson, B. 2009, ApJ, 702, 1413
Pont, F., Zucker, S., & Queloz, D. 2006, MNRAS, 373, 231
Rowe, J. F., et al. 2006, ApJ, 646, 1241
Sharp, C. M., & Burrows, A. 2007, ApJS, 168, 140
Showman, A. P., Cooper, C. S., Fortney, J. J., & Marley, M. S. 2008, ApJ, 682, 559
Sing, D. K., & López-Morales, M. 2009, A&A, 493, L31
Snellen, I. A. G., de Mooij, E. J. W., & Albrecht, S. 2009, Nature, 459, 543
Spiegel, D. S., Silverio, K., & Burrows, A. 2009, ApJ, 699, 1487
Sudarsky, D., Burrows, A., & Hubeny, I. 2003, ApJ, 588, 1121
Sudarsky, D., Burrows, A., & Pinto, P. 2000, ApJ, 538, 885
Swain, M. R., Vasisht, G., & Tinetti, G. 2008, Nature, 452, 329
Swain, M. R., Vasisht, G., Tinetti, G., Bouwman, J., Chen, P., Yung, Y., Deming, D., & Deroo, P. 2009, ApJ, 690, L114
Tamuz, O., Mazeh, T., & Zucker, S. 2005, MNRAS, 356, 1466
Tinetti, G., et al. 2007, Nature, 448, 169
Zahnle, K., Lodders, K., & Fortney, J. J. 2009a, AAS Meeting Abstracts, 214, 306.01
Zahnle, K., Marley, M. S., Lodders, K., & Fortney, J. J. 2009b, ApJ, 701, L20